Research Update: Interface-engineered oxygen octahedral tilts in perovskite oxide heterostructures

Daisuke Kan', Ryotaro Aso, Hiroki Kurata, and Yuichi Shimakawa

Citation: APL Materials **3**, 062302 (2015); doi: 10.1063/1.4918965
View online: http://dx.doi.org/10.1063/1.4918965
View Table of Contents: http://aip.scitation.org/toc/apm/3/6
Published by the American Institute of Physics

Research Update: Interface-engineered oxygen octahedral tilts in perovskite oxide heterostructures

Daisuke Kan,[1,a] Ryotaro Aso,[1] Hiroki Kurata,[1] and Yuichi Shimakawa[1,2]
[1]*Institute for Chemical Research, Kyoto University, Uji, Kyoto 611-0011, Japan*
[2]*Japan Science and Technology Agency, CREST, Uji, Kyoto 611-0011, Japan*

(Received 23 February 2015; accepted 12 April 2015; published online 22 April 2015)

Interface engineering of structural distortions is a key for exploring the functional properties of oxide heterostructures and superlattices. In this paper, we report on our comprehensive investigations of oxygen octahedral distortions at the heterointerface between perovskite oxides $SrRuO_3$ and $BaTiO_3$ on $GdScO_3$ substrates and of the influences of the interfacially engineered distortions on the magneto-transport properties of the $SrRuO_3$ layer. Our state-of-the-art annular bright-field imaging in aberration-corrected scanning transmission electron microscopy revealed that the RuO_6 octahedral distortions in the $SrRuO_3$ layer have strong dependence on the stacking order of the $SrRuO_3$ and $BaTiO_3$ layers on the substrate. This can be attributed to the difference in the interfacial octahedral connections. We also found that the stacking order of the oxide layers has a strong impact on the magneto-transport properties, allowing for control of the magnetic anisotropy of the $SrRuO_3$ layer through interface engineering. Our results demonstrate the significance of the interface engineering of the octahedral distortions on the structural and physical properties of perovskite oxides. [http://dx.doi.org/10.1063/1.4918965]

A broad spectrum of fascinating functional properties seen in heterointerfaces, which consist of dissimilar transition-metal oxides, has attracted much attentions.[1–7] Due to recent advances in atomic level synthesis technique, interface engineering[8–13] of oxides has emerged as a useful approach to explore and fine tune their functional properties. Because manipulating the interface is often associated with the added structural distortions, it is crucial to understand how the interfacial modification affects not only the structural but also the physical properties of entire constituent oxide layers. However, full understanding of the influence of interfacial distortions remains elusive because precise measurements of the positions of both cation and oxygen are required.

Cross-sectional imaging in aberration-corrected scanning transmission electron microscopy (STEM) has been shown to be useful for revealing oxygen octahedral distortions including deformations and tilts (or rotations) in oxide heterostructures.[14–21] The recent development of annular bright-field (ABF) imaging in STEM allows for simultaneous mapping of both light and heavy elements[22–24] and makes it possible to visualize oxygen coordination environments in the heterostructures.[18,25,26] Fast multiple-image acquisition and drift correction techniques using a cross correlation of the images[27] have been also demonstrated to minimize the image distortions due to drifts in both the specimen and incident probe in STEM, and consequently, the atomic positions for all constituent atoms—including oxygen—can be determined with sub-Ångström precision.[18,19,28]

In this article, we present our investigations of oxygen octahedral distortions in heterostructures consisting of perovskite oxides $SrRuO_3$ (SRO) and $BaTiO_3$ (BTO) grown on $GdScO_3$ (GSO) substrates and our investigations of their influences on the magneto-transport properties of the SRO layer. Our high-resolution STEM observations reveal that octahedral distortion in the SRO layer

[a]dkan@scl.kyoto-u.ac.jp

is strongly dependent on the stacking order of the SRO and BTO layers. When a SRO layer is deposited on a BTO layer, a tetragonal SRO layer with a negligibly small RuO_6 tilt is stabilized. In contrast, for a SRO layer with a BTO layer on top of it, the gradually changing octahedral tilts occur in the SRO layer, but a monoclinic structure is maintained. We also found that the magneto-transport properties of the SRO layer are closely correlated with the interfacially engineered RuO_6 octahedral distortions. Based on the experimental results, we discuss the structural and physical properties of the interfacially engineered SRO layer.

SRO (10 nm)/BTO (1.2 nm)/GSO and BTO (5 nm)/SRO (11 nm)/GSO heterostructures were fabricated by successively depositing SRO and BTO layers on $(110)_{ortho}$ GSO substrates using pulsed laser deposition. (The subscript *ortho* denotes the orthorhombic perovskite notation.) The thickness of each layer is indicated in parentheses. All depositions were carried out at a constant substrate temperature of 700 °C. The SRO and BTO layers were grown under oxygen pressures of 100 mTorr and 25 mTorr, respectively. The details of the growth conditions were given in our previous report.[20] For the cross-sectional observations, the fabricated heterostructures were thinned down to electron transparency by mechanical polishing and Ar-ion milling. The cross-sectional images were obtained using a spherical aberration-corrected STEM (JEM-9980TKP1; accelerating voltage = 200 kV, C_s = −0.025 nm, and C_5 = 15 mm) equipped with a cold field emission gun. The details of the image acquisition and analysis processes have been provided in our previous paper.[18] Figures 1 and 2 show typical cross-sectional high-angle annular dark-field (HAADF-) and

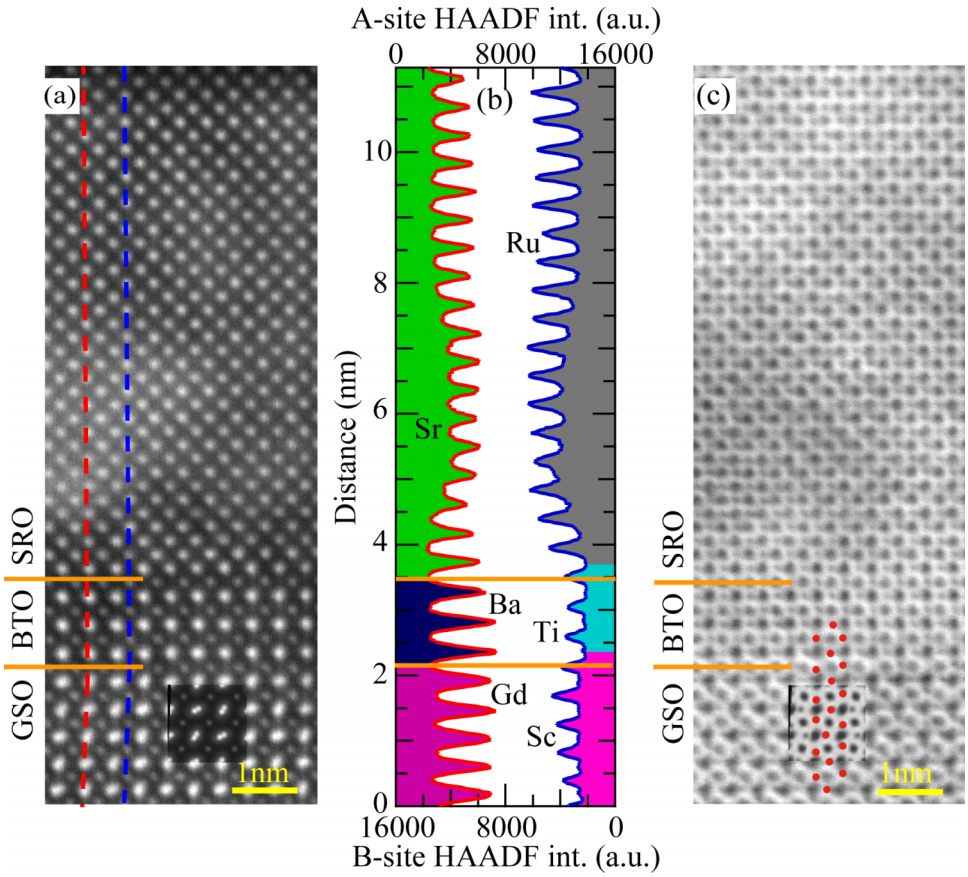

FIG. 1. HAADF- and ABF-STEM observations for the SRO (10 nm)/BTO (1.2 nm)/GSO heterostructure and element characterization. (a) High-resolution HAADF image taken along the $[001]_{ortho}$ direction. Simulated HAADF images of bulk GSO are inserted in the image. (b) HAADF intensity profiles of *A*- (left side) and *B*-site (right side) cations across the heterostructure. The *A*- and *B*-site profiles were collected along the red and blue lines in the HAADF image (Fig. 1(a)), respectively. The orange lines denote the positions of the BTO/GSO and SRO/BTO interfaces. (c) ABF image taken from the same region as the HAADF image (Fig. 1(a)). In the ABF image, the oxygen atoms (dotted in red) can be clearly seen.

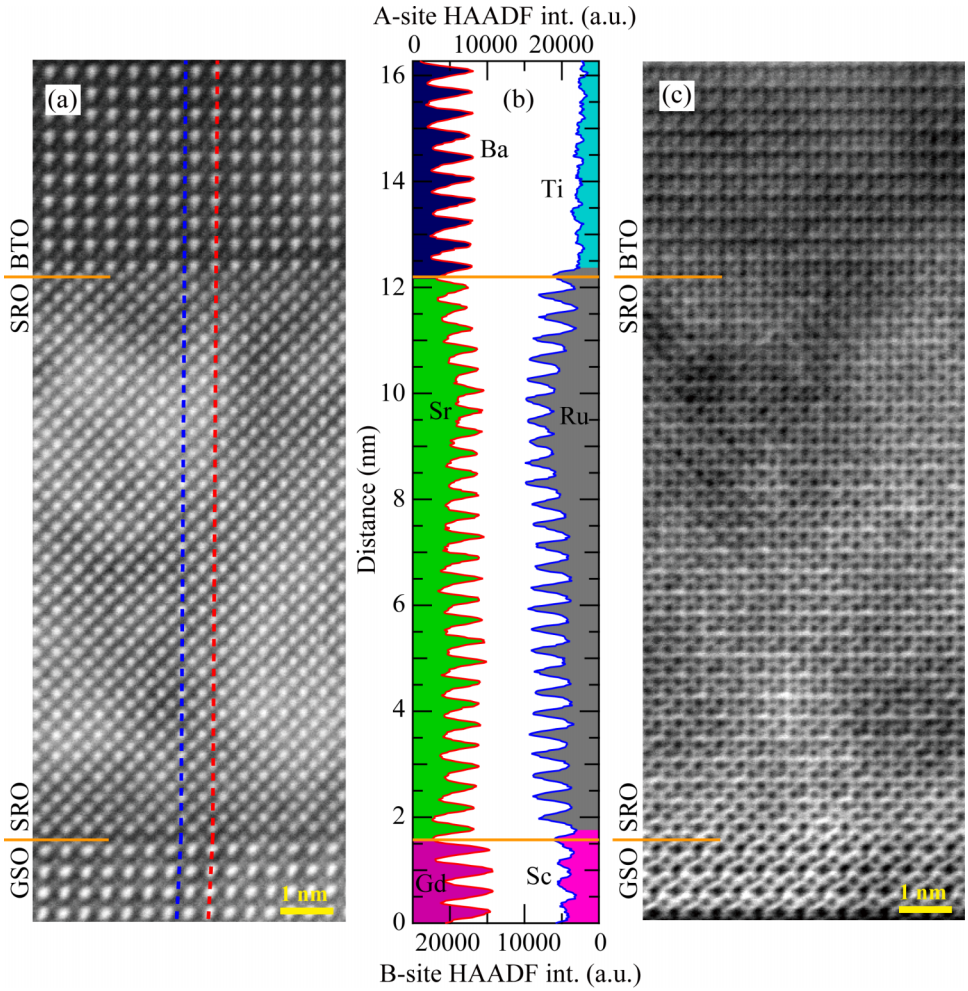

FIG. 2. HAADF- and ABF-STEM observations for the BTO (5 nm)/SRO (11 nm)/GSO heterostructure and element characterization. (a) High-resolution HAADF image taken along the $[001]_{ortho}$ direction. (b) HAADF intensity profiles of *A*- (left side) and *B*-site (right side) cations across the heterostructure. The *A*- and *B*-site profiles were collected along the red and blue lines in the HAADF image (Fig. 2(a)), respectively. The orange lines denote the positions of the SRO/GSO and BTO/SRO interfaces. (c) ABF image taken from the same region as the HAADF image (Fig. 2(a)). In the ABF image, the oxygen atoms can be clearly seen.

ABF-STEM images of the SRO (10 nm)/BTO (1.2 nm)/GSO and BTO (5 nm)/SRO (11 nm)/GSO heterostructures, respectively. In the HAADF images, no misfit dislocations can be seen in each heterointerface, demonstrating coherent growth in both the SRO and BTO layers on the substrates independent of the stacking sequence. The results of the x-ray reciprocal space mapping[18,29] corroborate this finding. The HAADF intensity profiles in Figs. 1(b) and 2(b) show that each interface has an abrupt change in the *A*- and *B*-site cation HAADF intensities and that each interface is terminated by the *B*-site BO_2 layer (*B* = Sc, Ru, and Ti). These findings indicate that interfacial cation mixing is unlikely and that the *B*-site terminations are preserved in both SRO (10 nm)/BTO (1.2 nm)/GSO and BTO (5 nm)/SRO (11 nm)/GSO heterostructures. These observations ensure high quality of our fabricated heterostructures. In the ABF images (Figs. 1(c) and 2(c)), where the constituent atoms can be observed as dark contrast,[22–24] we can clearly see not only the cation but also oxygen atomic columns, providing information on octahedral distortions and connections across the heterostructures.

To understand the influences of the BTO bottom and upper layers on the SRO layer structure, we evaluated the oxygen octahedral tilt angle θ_{tilt} and in-plane oxygen displacement Δx as a function of the atomic position in the heterostructures. With the ABF-STEM images, the θ_{tilt} and Δx

were determined from the oxygen atom positions that were extracted with Bragg filtering and cubic interpolation techniques in the "Find Peaks" option of the HREM Research Peak Pairs Analysis software package.[30,31] The results for the SRO (10 nm)/BTO (1.2 nm)/GSO and BTO (5 nm)/SRO (11 nm)/GSO heterostructures are shown in Figures 3(a) and 4, respectively. The definitions of the θ_{tilt} and Δx are also shown in Fig. 3. We note that θ_{tilt} used in this study corresponds to the tilt angle projected on the $(001)_{\text{ortho}}$ plane. For comparison, the tilt angle and in-plane oxygen displacement in the SRO (15 nm)/GSO heterostructure, of which the SRO layer has a monoclinic structure,[18,20,32] are included in Fig. 3(b). For the SRO/BTO/GSO heterostructure (Fig. 3(a)), the octahedral tilt is strongly suppressed across the BTO/GSO interface. The θ_{tilt} changes from 156° in the substrate region to 180° in the three unit-cell-thick BTO layer. Consequently, the θ_{tilt} at the interface between the SRO and BTO layers is 180°, and the RuO_6 octahedra in the SRO layer have negligibly small tilts, indicating that the SRO layer in the SRO/BTO/GSO heterostructure has a tetragonal structure.[32] The observed behavior is in contrast to that of the SRO/GSO heterostructure shown in Fig. 3(b). The SRO/GSO heterostructure has only a slight decrease in the tilt angle across the interface, and the SRO layer maintains the octahedral tilts comparable to those in the bulk counterpart, indicating that the SRO layer has the monoclinic structure. The results indicate that the BTO layer inserted between SRO and GSO results in the structural change in the SRO layer from the monoclinic phase to the tetragonal one.

The observed structural changes due to the insertion of the BTO layer can be attributed to changes in the octahedral connection at the interface. For the SRO/BTO/GSO heterostructure, the in-plane displacement Δx of oxygen atoms, which is directly related to the octahedral tilt, is significantly reduced at the BTO/GSO interface and decreases to 0 pm within the three unit-cell-thick BTO layer, as shown in Fig. 3(a). The results indicate that a RuO_6-TiO_6 octahedral connection with negligibly small tilts is formed at the SRO/BTO interface and that the propagation of the octahedral tilt from the GSO substrate into the SRO layer is blocked by the three unit-cell-thick BTO layer, stabilizing the tetragonal SRO structure. However a Δx as large as 26 pm is maintained at the SRO/GSO interface (Fig. 3(b)), and the tilted RuO_6 and ScO_6 are connected, facilitating the propagation of the octahedral tilts and consequently stabilizing the monoclinic SRO structure. These results indicate that the BTO layer inserted underneath the SRO layer modifies the interfacial octahedral connections associated with the change in the oxygen displacement, thereby determining the structural phase of the SRO layer.

For the BTO/SRO/GSO heterostructure (Fig. 4), the RuO_6 octahedral tilt, which remains comparable to the bulk counterpart near the SRO/GSO interface, undergoes a gradual decrease toward the BTO layer and is completely suppressed at the upper BTO/SRO interface. Although the SRO layer in the BTO/SRO/GSO heterostructure has a structure very close to the monoclinic structure seen in the SRO/GSO heterostructure, the observed behavior in the octahedral tilt is in stark contrast to those for the SRO/GSO heterostructures (Fig. 3(b)), in which the SRO layer has the almost constant octahedral tilt. Interestingly, the inversion symmetry of the SRO layer of the BTO/SRO/GSO heterostructure is broken by the gradual change in the tilt angle, while the inversion symmetry of the SRO layer with the constant tilt—seen either in bulk or in the SRO/GSO heterostructure—is maintained. The results indicate that the introduction of the spatially *inhomogeneous* structural distortions through the interface engineering is a good way to stabilize oxides with structural symmetry not seen in bulk.

The oxygen displacement in Fig. 4 also shows the concomitant changes with the gradual decrease in the tilts. A large displacement of ~29 pm at the SRO/GSO interface shows that the interfacial octahedral connection consists of the tilted RuO_6 and ScO_6 octahedra. However, the displacement at the BTO/SRO interface is largely suppressed to ~2 pm, indicating that the RuO_6 octahedra with negligibly small tilts are connected to non-tilted TiO_6. We ascribed the gradually changing RuO_6 tilts to the difference in the octahedral connection angle between the SRO/GSO and BTO/SRO interfaces. Given that the oxygen displacement at the interface determines the degree of the tilt propagation,[19] the top BTO layer, which suppresses the RuO_6 tilts induced by the tilt propagation from the substrate, influences the octahedral tilts in the underneath SRO layer through the interfacial octahedral connection, thus stabilizing the gradually changing RuO_6 tilt in the BTO/SRO/GSO heterostructure. It is interesting to compare the behavior of octahedral tilts

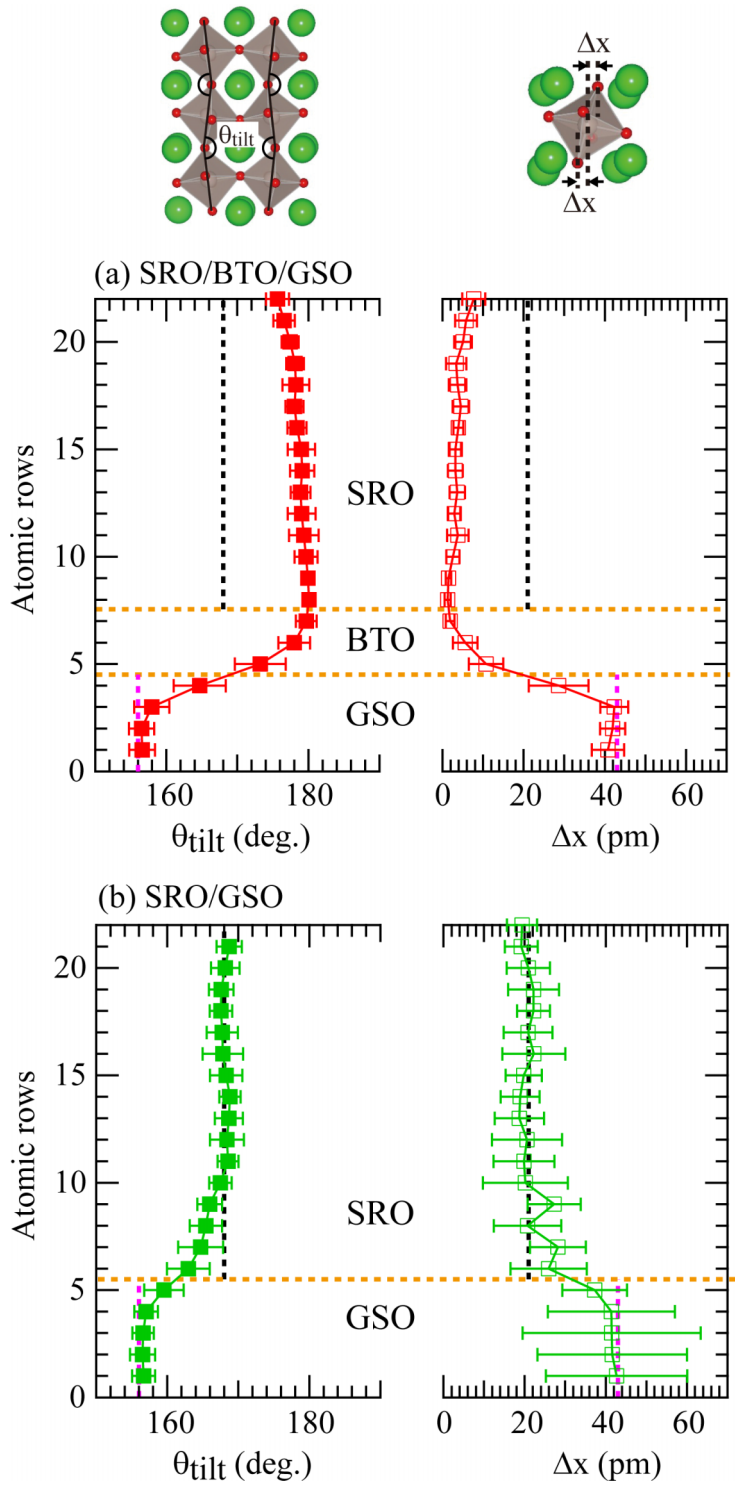

FIG. 3. Evaluations of octahedral distortions in the SRO (10 nm)/BTO (1.2 nm)/GSO heterostructure. (a) Variations in octahedral tilt angle θ_{tilt} (filled red squares) and in-plane oxygen displacement Δx (open red squares) in the SRO/BTO/GSO heterostructure. (b) θ_{tilt} and Δx of the SRO (15 nm)/GSO heterostructure (green) in which SRO layer has the monoclinic structure. We note that θ_{tilt} used in this study corresponds to the tilt angle projected on the $(001)_{ortho}$ plane. The error bars correspond to the standard deviation of each of the determined values. The values of θ_{tilt} and Δx of bulk SRO ($a_{pc\_SRO} = 3.92$ Å, $\theta_{tilt\_SRO} = 168°$)[37] and GSO ($a_{pc\_GSO} = 3.96$ Å, $\theta_{tilt\_GSO} = 156°$)[38] are indicated by black and pink lines, respectively. The orange dashed lines represent the positions of the interfaces. The subscript *pc* denotes the pseudo-cubic perovskite notation.

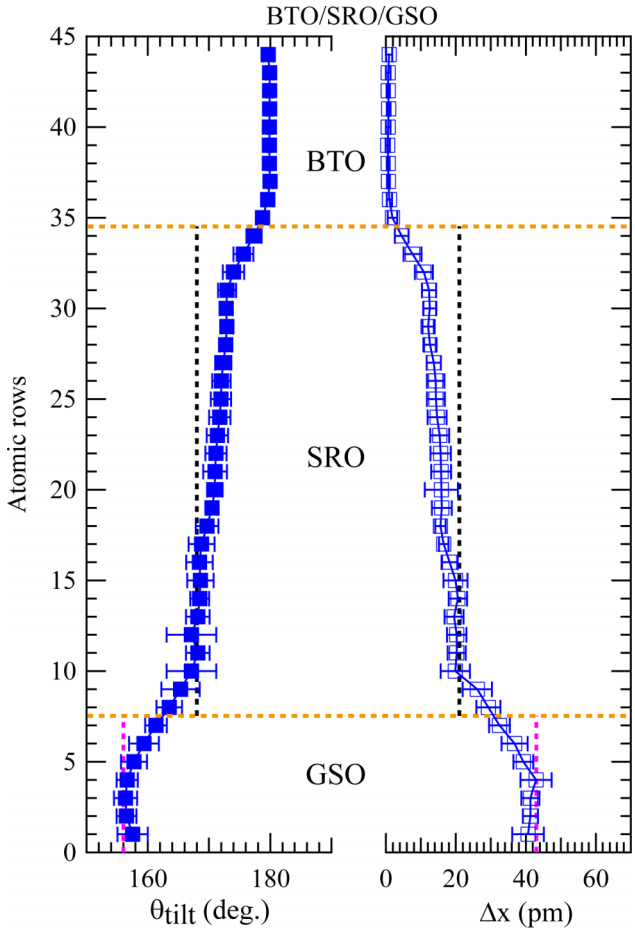

FIG. 4. Evaluations of octahedral distortions in the BTO (5 nm)/SRO (11 nm)/GSO heterostructure. Variations in octahedral tilt angle θ_{tilt} (filled square) and in-plane oxygen displacement Δx (open square) in the BTO/SRO/GSO heterostructure. The error bars correspond to the standard deviation of each of the determined values. The values of θ_{tilt} and Δx of bulk SRO[37] and GSO[38] are indicated by black and pink lines, respectively. The orange dashed lines represent the positions of the BTO/SRO and SRO/GSO interfaces.

between the BTO/SRO/GSO and BTO/GSO[19] heterostructures. While the BTO layers in both heterostructures stabilize the interfacial octahedral connections with the suppressed oxygen displacement (the TiO_6-RuO_6 connection for BTO/SRO/GSO and the TiO_6-ScO_6 one for BTO/GSO), the gradual change in the octahedral tilt is seen only in the BTO/SRO/GSO heterostructure. This observation implies that while the octahedral connection angle at the interface is controlled by the *A*-site cation size,[19] the number of the octahedral layer whose octahedral tilt can be modified through the interfacial octahedral connection strongly depends on the relative size mismatch between the *A*- and *B*-site cations in the constituent layer (Sr and Ru for SRO and Gd and Sc for GSO), which is in principle characterized by the Goldschmidt tolerance factor.[33–36] Given that the tolerance factor of SRO (0.994) is close to unity, the results suggest that perovskite oxides whose *A*- and *B*-site cations size mismatch is relatively small, preferentially accommodates spatially *inhomogeneous* structural distortions.

To evaluate the influences of the interfacially engineered RuO_6 octahedral tilts on the functional properties, we investigated the magneto-transport properties of the SRO/BTO/GSO and BTO/SRO/GSO heterostructures. The obtained data are summarized in Fig. 5. Regardless of the BTO layer, all heterostructures exhibit metallic conductions down to 10 K and undergo ferromagnetic transitions at 110-140 K, which can be seen as humps in the ρ_{xx}-T curves (Fig. 5(a)). We note no clear relationships between the transition temperature (T_c) and interface structure. The

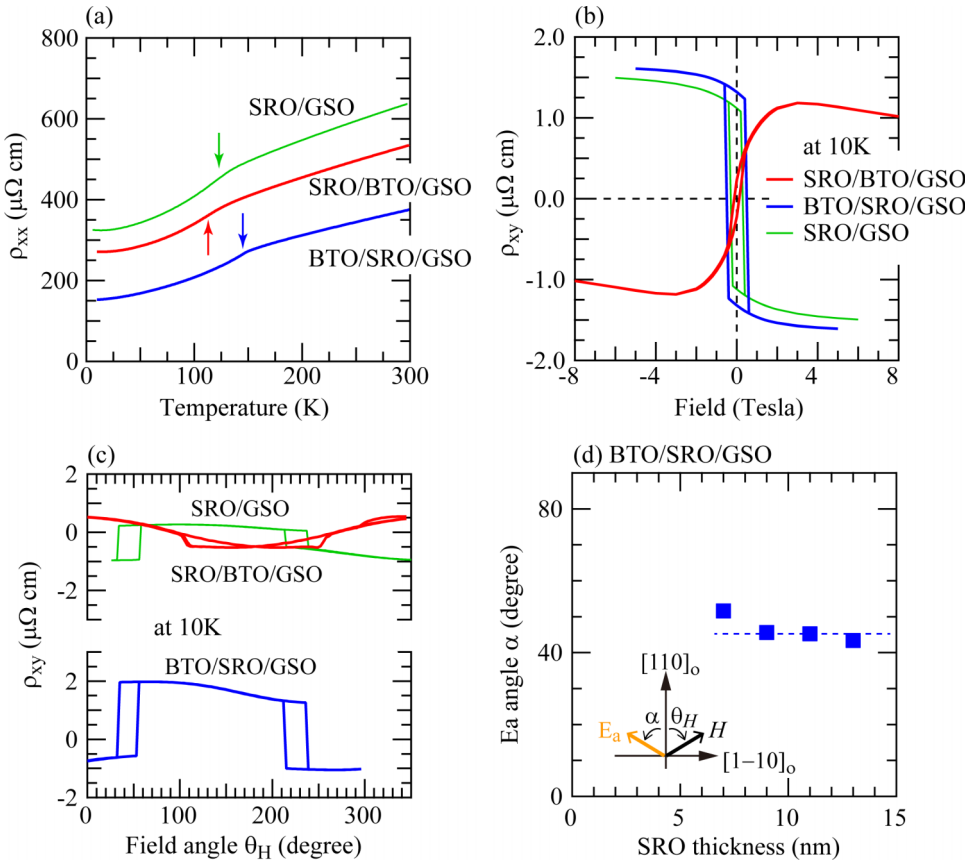

FIG. 5. Magneto-transport characterization of the interface-engineered heterostructures. (a) Temperature dependence of electrical resistivity ρ_{xx} of the SRO (10 nm)/BTO (1.2 nm)/GSO and BTO (5 nm)/SRO (11 nm)/GSO heterostructures. The arrows in the figure denote the ferromagnetic transition temperature for each heterostructure. (b) Typical magnetic field dependence of Hall resistivity ρ_{xy} of the SRO/BTO/GSO and BTO/SRO/GSO heterostructures. The data were taken at 10 K. For the measurements, the current and magnetic field were applied along the $[001]_{ortho}$ and $[110]_{ortho}$ directions, respectively. (c) Magnetic field angle θ_H dependence of the Hall resistivity ρ_{xy} of SRO (10 nm)/BTO (1.2 nm)/GSO (upper) and BTO (5 nm)/SRO (11 nm)/GSO (bottom) heterostructures. The data were taken under the current along the $[001]_{ortho}$ direction and the magnetic field in the $(001)_{ortho}$ plane. (d) Magnetic easy axis (E_a) direction α of SRO layer in the BTO (5 nm)/SRO (t_{SRO})/GSO heterostructure ($t\_{SRO} = 7$, 9, 11, and 13 nm) as a function of the SRO layer thickness t_{SRO}. The definitions of θ_H and α are shown in the figure.

magnetic field dependence of the Hall resistivity ρ_{xy} in Fig. 5(b) reveals a strong influence of the stacking order of the heterostructure on the magnetic anisotropy of the SRO layer. The anomalous part in ρ_{xy} for the SRO/BTO/GSO heterostructure shows no hysteresis, which is characteristic of the in-plane magnetic anisotropy. In contrast, a clear hysteresis due to the reversal of the magnetic moment is seen for the anomalous part in ρ_{xy} of the SRO/GSO and BTO/SRO/GSO heterostructures, indicating that the magnetic moment has a component along the out-of-plane ($[110]_{GSO}$) direction.

To further determine the direction of the magnetic easy axis E_a of the SRO layer, we measured the dependence of ρ_{xy} on the magnetic field angle θ_H. The results are shown in Fig. 5(c). Clear jumps with the hysteresis in the clockwise and counter-clockwise field rotations due to the field-induced magnetization reversal are seen. A jump in ρ_{xy} is observed at every 180° in θ_H, revealing the uniaxial magnetic anisotropy of the SRO layer in all heterostructures. From the center angle of the hysteresis, the E_a angle α is determined to be ~90° for SRO/BTO/GSO, ~45° for BTO/SRO/GSO, and ~45° for SRO/GSO. Figure 5(d) shows α as a function of the thickness of the SRO layer in the BTO/SRO/GSO heterostructure. While the SRO layer has various degrees of the RuO_6 tilt, α remains ~45° independent of the SRO layer thickness, indicating little influence of the gradually

changing tilt angle on the magnetic anisotropy. We also note that α is independent of both temperature and the thickness of the BTO layer for all heterostructures. Our observation indicates that α is determined by the SRO layer's structure, highlighting the significant role of the magnetocrystalline effect on the magnetic anisotropy.

In summary, we demonstrated that the interface engineering is useful in controlling oxygen octahedral distortions in oxide heterostructures. We showed that the RuO_6 octahedral distortions in the SRO epitaxial layer on the GSO substrate can be engineered by adding a thin (a few unit cell thick) BTO layer either underneath or above the SRO layer. The BTO layer inserted underneath the SRO layer induces the monoclinic-to-tetragonal structural phase transition associated with the large suppression in the RuO_6 octahedral tilt. The BTO layer on the SRO layer, on the other hand, stabilizes the gradually changing RuO_6 tilts across the SRO layer, leading to the broken inversion symmetry. We ascribed the observed distortions to the interfacial octahedral connections modified by the added BTO layer. We also investigated the influence of interface engineering on the magneto-transport properties of the SRO layer, revealing that the magnetic anisotropy is controlled by the interfacially engineered RuO_6 octahedral distortions through the magnetocrystalline effect. The results imply that the interface engineering enables accommodating various types of octahedral distortions, specifically, oxygen coordination environments that are strongly correlated with functional properties such as dielectric and magnetic properties and metal-insulator transitions. Designing and stabilizing oxygen coordination environments not seen in bulk materials would allow for exploring novel phenomena emergent in oxide heterostructures.

This work was partially supported by a grant for the Joint Project of Chemical Synthesis Core Research Institutions from the Ministry of Education, Culture, Sports, Science, and Technology of Japan. The work was also supported by the Japan Science and Technology Agency, CREST.

[1] D. G. Schlom, L.-Q. Chen, C.-B. Eom, K. M. Rabe, S. K. Streiffer, and J.-M. Triscone, Annu. Rev. Mater. Res. **37**, 589 (2007).
[2] J. M. Rondinelli and N. A. Spaldin, Adv. Mater. **23**, 3363 (2011).
[3] M. Bibes, J. E. Villegas, and A. Barthélémy, Adv. Phys. **60**, 5 (2011).
[4] P. Zubko, S. Gariglio, M. Gabay, P. Ghosez, and J.-M. Triscone, Annu. Rev. Condens. Matter Phys. **2**, 141 (2011).
[5] H. Y. Hwang, Y. Iwasa, M. Kawasaki, B. Keimer, N. Nagaosa, and Y. Tokura, Nat. Mater. **11**, 103 (2012).
[6] A. Bhattacharya and S. J. May, Annu. Rev. Mater. Res. **44**, 65 (2014).
[7] J. Chakhalian, J. W. Freeland, A. J. Millis, C. Panagopoulos, and J. M. Rondinelli, Rev. Mod. Phys. **86**, 1189 (2014).
[8] R. Maran, S. Yasui, E. A. Eliseev, M. D. Glinchuk, A. N. Morozovska, H. Funakubo, I. Takeuchi, and V. Nagarajan, Phys. Rev. B **90**, 245131 (2014).
[9] H. W. Jang, D. A. Felker, C. W. Bark, Y. Wang, M. K. Niranjan, C. T. Nelson, Y. Zhang, D. Su, C. M. Folkman, S. H. Baek, S. Lee, K. Janicka, Y. Zhu, X. Q. Pan, D. D. Fong, E. Y. Tsymbal, M. S. Rzchowski, and C. B. Eom, Science **331**, 886 (2011).
[10] Y.-M. Kim, A. Kumar, A. Hatt, A. N. Morozovska, A. Tselev, M. D. Biegalski, I. Ivanov, E. A. Eliseev, S. J. Pennycook, J. M. Rondinelli, S. V. Kalinin, and A. Y. Borisevich, Adv. Mater. **25**, 2497 (2013).
[11] Z. H. Chen, A. R. Damodaran, R. Xu, S. Lee, and L. W. Martin, Appl. Phys. Lett. **104**, 182908 (2014).
[12] H. Lu, X. Liu, J. D. Burton, C. W. Bark, Y. Wang, Y. Zhang, D. J. Kim, A. Stamm, P. Lukashev, D. A. Felker, C. M. Folkman, P. Gao, M. S. Rzchowski, X. Q. Pan, C. B. Eom, E. Y. Tsymbal, and A. Gruverman, Adv. Mater. **24**, 1209 (2012).
[13] Y. W. Yin, J. D. Burton, Y. M. Kim, A. Y. Borisevich, S. J. Pennycook, S. M. Yang, T. W. Noh, A. Gruverman, X. G. Li, E. Y. Tsymbal, and Q. Li, Nat. Mater. **12**, 397 (2013).
[14] A. Y. Borisevich, H. J. Chang, M. Huijben, M. P. Oxley, S. Okamoto, M. K. Niranjan, J. D. Burton, E. Y. Tsymbal, Y. H. Chu, P. Yu, R. Ramesh, S. V. Kalinin, and S. J. Pennycook, Phys. Rev. Lett. **105**, 087204 (2010).
[15] A. Y. Borisevich, O. S. Ovchinnikov, H. J. Chang, M. P. Oxley, P. Yu, J. Seidel, E. A. Eliseev, A. N. Morozovska, R. Ramesh, S. J. Pennycook, and S. V. Kalinin, ACS Nano **4**, 6071 (2010).
[16] J. Y. Zhang, J. Hwang, S. Raghavan, and S. Stemmer, Phys. Rev. Lett. **110**, 256401 (2013).
[17] Z. Wang, L. Gu, M. Saito, S. Tsukimoto, M. Tsukada, F. Lichtenberg, Y. Ikuhara, and J. G. Bednorz, Adv. Mater. **25**, 218 (2013).
[18] R. Aso, D. Kan, Y. Shimakawa, and H. Kurata, Sci. Rep. **3**, 2214 (2013).
[19] R. Aso, D. Kan, Y. Shimakawa, and H. Kurata, Cryst. Growth Des. **14**, 2128 (2014).
[20] R. Aso, D. Kan, Y. Shimakawa, and H. Kurata, Adv. Funct. Mater. **24**, 5177 (2014).
[21] E. J. Moon, R. Colby, Q. Wang, E. Karapetrova, C. M. Schlepütz, M. R. Fitzsimmons, and S. J. May, Nat. Commun. **5**, 5710 (2014).
[22] S. D. Findlay, N. Shibata, H. Sawada, E. Okunishi, Y. Kondo, T. Yamamoto, and Y. Ikuhara, Appl. Phys. Lett. **95**, 191913 (2009).
[23] S. D. Findlay, N. Shibata, H. Sawada, E. Okunishi, Y. Kondo, and Y. Ikuhara, Ultramicroscopy **110**, 903 (2010).
[24] M. Haruta and H. Kurata, Sci. Rep. **2**, 252 (2012).
[25] R. Huang, H.-C. Ding, W.-I. Liang, Y.-C. Gao, X.-D. Tang, Q. He, C.-G. Duan, Z. Zhu, J. Chu, C. A. J. Fisher, T. Hirayama, Y. Ikuhara, and Y.-H. Chu, Adv. Funct. Mater. **24**, 793 (2014).

[26] D. Samal, T. Haiyan, H. Molegraaf, B. Kuiper, W. Siemons, S. Bals, J. Verbeeck, G. Van Tendeloo, Y. Takamura, E. Arenholz, C. A. Jenkins, G. Rijnders, and G. Koster, Phys. Rev. Lett. **111**, 096102 (2013).
[27] M. Saito, K. Kimoto, T. Nagai, S. Fukushima, D. Akahoshi, H. Kuwahara, Y. Matsui, and K. Ishizuka, J. Electron Microsc. **58**, 131 (2009).
[28] R. Aso, D. Kan, Y. Fujiyoshi, Y. Shimakawa, and H. Kurata, Cryst. Growth Des. **14**, 6478 (2014).
[29] D. Kan, R. Aso, H. Kurata, and Y. Shimakawa, J. Appl. Phys. **115**, 184304 (2014).
[30] P. L. Galindo, S. Kret, A. M. Sanchez, J.-Y. Laval, A. Yáñez, J. Pizarro, E. Guerrero, T. Ben, and S. I. Molina, Ultramicroscopy **107**, 1186 (2007).
[31] J. Pizarro, P. Galindo, S. Molina, and K. Ishizuka, Microsc. Anal. **23**, 23 (2009).
[32] D. Kan, R. Aso, H. Kurata, and Y. Shimakawa, Adv. Funct. Mater. **23**, 1129 (2013).
[33] V. M. Goldschmidt, Naturwissenschaften **14**, 477 (1926).
[34] P. M. Woodward, Acta Crystallogr., Sect. B: Struct. Sci. **53**, 32 (1997).
[35] P. Woodward, Acta Crystallogr., Sect. B: Struct. Sci. **53**, 44 (1997).
[36] J. B. Goodenough, Rep. Prog. Phys. **67**, 1915 (2004).
[37] C. W. Jones, P. D. Battle, P. Lightfoot, and W. T. A. Harrison, Acta Crystallogr., Sect. C: Cryst. Struct. Commun. **45**, 365 (1989).
[38] R. P. Liferovich and R. H. Mitchell, J. Solid State Chem. **177**, 2188 (2004).